mining

MDPI

Article

Estimation of Critical Distances for Electronic Detonators Using a Physics-Based Model

Alejandro Díaz [1,2], Luis Álvarez [3,4], Carlos Toledo [4], Elisabete Alberdi [2] and Heber Hernández [3,4,*]

[1] Orica S.A., Av. Costanera Sur 2730, 3rd Floor, Las Condes, Santiago 8370003, Chile; alejandro.diaz2@orica.com
[2] Department of Applied Mathematics, University of the Basque Country UPV/EHU, 48013 Bilbao, Spain; elisabete.alberdi@ehu.eus
[3] Facultad de Ingeniería y Negocios, Universidad Santo Tomás, Ejército Libertador 146, Santiago 8370003, Chile; lalvarez10@santotomas.cl
[4] MSMP Research Group, Ejército Libertador 146, Santiago 8370003, Chile; ctoledo15@santotomas.cl
* Correspondence: hhernandez9@santotomas.cl

Abstract

Prior estimation of the distance at which detonation pressure reaches a critical threshold is relevant for defining borehole separations and reducing the risk of damage to electronic detonators in underground mining. Empirical attenuation relationships require site-specific calibration through instrumentation, limiting their application at preliminary design stages. A physics-based formulation is proposed that integrates detonation pressure, explosive–rock impedance matching, and equivalent rock mass stiffness to estimate transmitted pressure and critical distance. Attenuation is represented by an exponent defined from the relative dynamic demand, expressed as the ratio between the initially transmitted pressure and the equivalent deformation modulus. The model was evaluated using experimental data from El Teniente, Chuquicamata Underground, and Pucobre. Across five experimental conditions, the estimates yielded a mean absolute relative error of 8.43% and a root mean square error of 0.101 m. The results show that critical distance depends on the interaction among explosive properties, impedance contrast, and rock mass stiffness, rather than exclusively on rock mass rating. The formulation provides a tool for preliminary estimation of safety separations, although broader experimental validation is required to establish its general applicability.

Keywords: underground blasting; detonation pressure; critical distance; explosive–rock impedance matching; rock mass; electronic detonators

Check for updates

Academic Editors: Mohammad H.B. (Farzine) Nasseri and Bibhu Mohanty

Received: 14 August 2026
Revised: 11 September 2026
Accepted: 1 October 2026
Published: 5 October 2026

Copyright: © 2026 by the authors. Licensee MDPI, Basel, Switzerland. This article is an open access article distributed under the terms and conditions of the Creative Commons Attribution (CC BY) license.

1. Introduction

Explosive detonation releases energy that is transferred to the rock mass through shock waves, stress waves, and gas expansion [1]. This energy transfer governs processes such as fragmentation, blast-induced damage, and the dynamic response of excavations. Consequently, estimating the transmission and attenuation of blast-induced dynamic disturbances is relevant to drilling and charging design, damage control, and the definition of safety criteria in underground mining [2]. In deep underground operations, the interaction among high-stress states, heterogeneous geomechanical conditions, and high-precision initiation sequences increases the need to adequately characterize the propagation and superposition of the blast-induced dynamic response [3]. In addition, the dynamic loading generated by a previously detonated borehole may propagate toward adjacent boreholes and affect the integrity or performance of electronic detonators that have not yet been initiated [4]. Therefore, critical distance is defined in this study as the separation from the donor borehole

at which the transmitted dynamic pressure decreases to a specified operational threshold. Its prior estimation is of both scientific and practical interest because it can provide relevant information for defining spatial constraints and coordinating activities in short-term underground mine planning [5], particularly when instrumentation campaigns are not available for the sector under analysis.

The attenuation of blast-induced dynamic response has traditionally been described using empirical power-law relationships. Among the most widely used formulations are those proposed by [6] and the subsequent developments by [7], based primarily on peak particle velocity (PPV) measurements and scaled distance. Although these formulations are typically expressed in terms of vibration, they represent the predominant empirical approach for characterizing the decay of rock mass dynamic response with distance. Their application requires site-specific coefficients to be determined through monitoring and experimental fitting [8], which limits their use in operations without prior information or during preliminary design stages [9,10]. In parallel, analytical, experimental, and numerical models have investigated the initial transfer of energy from the explosive to the rock and its subsequent propagation through the rock mass [11]. The efficiency of this transfer depends on the pressure generated by the explosive, dynamic coupling at the explosive–rock interface, and medium properties such as density, wave propagation velocity, and characteristic impedance [12,13]. Recent studies further show that stiffness, discontinuities, structural heterogeneity, and rock mass strength properties govern wave transmission, reflection, and dissipation [14–18].

Rock mass classification systems, such as the Rock Mass Rating (RMR) proposed by Bieniawski [19], characterize rock mass quality and support correlations for estimating equivalent mechanical properties. However, RMR alone does not describe dynamic response. Rock masses with similar ratings may differ in intact-rock stiffness, fracturing, and impedance, modifying pressure transmission and attenuation [20]. A representation of wave propagation should therefore incorporate mechanical properties as well as the geomechanical classification [21]. In this study, the equivalent mechanical representation consists of the intact-rock Young's modulus E_i and RMR combined into an equivalent rock mass deformation modulus E_{mr} through Equation (8). Discontinuity effects enter through this aggregate stiffness reduction; individual joint geometries and separate joint correction factors are not resolved. Rock density and P-wave velocity independently enter the impedance calculation. A remaining challenge is to estimate a distance associated with a pressure threshold before site-specific attenuation measurements become available.

Within this framework, the working hypothesis is that a formulation based on explosive–rock impedance matching and an equivalent mechanical representation of the rock mass can reproduce the critical distances observed under contrasting lithological and geomechanical conditions without requiring the calibration of site-specific empirical attenuation coefficients. Accordingly, the objective of this study is to develop and evaluate a physical model for estimating the dynamic pressure transmitted through the rock mass and determining the critical distance corresponding to a predefined operational threshold. The model was compared with observations from Chuquicamata Underground, El Teniente, and Pucobre to assess its ability to represent the dynamic response under different lithological and geomechanical conditions.

Recent work provides complementary approaches to this problem. He et al. [22] systematically reviewed tunnel blasting research, including design, monitoring, and modeling. Zhu et al. [23] used maximum-velocity mapping to predict damage in underground destress blasting, emphasizing near-field PPV and charge interactions. Zhou et al. [24] investigated Bayesian-network and random-forest models for blast-induced ground vibration, whereas Stochino et al. [25] developed a probabilistic blast-demand model and fragility functions

for industrial tanks. These studies address wave response or structural damage but do not directly establish pressure tolerances for electronic detonators. The present formulation instead estimates the distance associated with an externally specified dynamic-pressure threshold.

Machine learning also offers tools for approximating nonlinear mechanical responses. Drosopoulos and Stavroulakis [26] applied a deep operator network (DeepONet) to the failure response of a two-dimensional fiber-reinforced composite plate using finite-element-generated data. Bardhan and Kardani [27] developed a meta-ensemble model for Poisson's ratio and maximum horizontal stress in casing-collapse assessment. These examples illustrate possible surrogate-modeling approaches rather than the direct validation of blast-pressure attenuation. Their dependence on representative training data motivates the complementary use of an explicit, low-input formulation when field datasets are limited.

The remainder of this manuscript is organized as follows. Section 2 presents the model formulation, study sites, and field tests. Section 3 reports the input properties, comparisons with field observations, and parametric analysis. Section 4 discusses the physical interpretation, operational scope, and limitations. Section 5 presents the conclusions and directions for further validation.

2. Materials and Methods

2.1. Theoretical Basis of the Model

The proposed model is based on the principle that explosive detonation generates an initial dynamic pressure that is transmitted into the rock mass as shock and stress waves. During propagation, the pressure magnitude decreases with distance as a result of mechanisms including geometric spreading, reflection and refraction at discontinuities, deformation of the medium, and dissipation associated with rock mass fracturing and microfracturing. Consequently, the pressure reaching a given point depends primarily on the magnitude of the pressure generated by the explosive, pressure-amplitude transmission at the explosive–rock interface, and the capacity of the rock mass to transmit and attenuate the wave during propagation. Traditionally, the propagation of pressure or blast-induced vibration has been represented using power-law attenuation relationships, in which pressure decreases with distance according to an empirical exponent associated with rock mass behavior [6].

$$P = P_d \cdot \left(\frac{r}{d}\right)^n, \tag{1}$$

where P is the dynamic pressure at the point of interest, P_d is the detonation pressure in the borehole, r is the borehole radius, d is the distance measured from the borehole center, and n is the empirical attenuation exponent of the rock mass. In this type of formulation, higher n values represent a more rapid decrease in pressure amplitude with distance, a behavior that may be related to medium deformability, fracturing, discontinuities, and structural heterogeneity of the rock mass.

Although this type of formulation remains widely used to describe the propagation of blast-induced waves, determining the exponent n generally requires instrumentation campaigns and calibration against field measurements. This dependence on experimentally fitted parameters limits its application in deposits lacking monitoring records or when preliminary design scenarios must be evaluated.

The present study retains a power-law propagation structure and calculates its exponent from properties of the explosive and rock mass. The initially transmitted pressure is estimated through impedance matching, while attenuation depends on the ratio of transmitted pressure to equivalent rock mass stiffness. The formulation combines physically motivated relationships with an empirical stiffness correlation and an assumed attenuation function; it does not require fitting a separate attenuation exponent to each site.

2.2. Initial Pressure and Wave Transmission at the Explosive–Rock Interface

The pressure generated during detonation constitutes the initial condition for wave propagation into the rock mass. Its magnitude depends primarily on explosive density and velocity of detonation (VoD). The fraction of pressure amplitude transferred into the rock depends on the impedance contrast between the two media. The characteristic impedance of the explosive is defined as

$$Z_e = \rho_e \cdot VoD, \tag{2}$$

where Z_e is the characteristic impedance of the explosive and ρ_e is its density. Similarly, the characteristic impedance of the rock is expressed as

$$Z_r = \rho_r \cdot V_p, \tag{3}$$

where Z_r is the rock impedance, ρ_r is its density, and V_p is the compressional-wave propagation velocity. To represent the characteristic pressure associated with the detonation state, an approximation of the Chapman–Jouguet pressure (P_{CJ}) for condensed explosives is adopted:

$$P_{CJ} = \frac{\rho_e \cdot VoD^2}{4}. \tag{4}$$

This formulation distinguishes the physical detonation pressure from the quantity $\rho_e \cdot VoD^2$, which represents a pressure scale but does not, by itself, correspond to the Chapman–Jouguet pressure.

When a wave reaches the interface between two media with different impedances, part of its amplitude is reflected and part is transmitted. Under the assumptions of normal incidence and locally elastic behavior, the pressure-amplitude transmission coefficient from the explosive to the rock is expressed as

$$T_p = \frac{2Z_r}{(Z_e + Z_r)}, \tag{5}$$

where T_p is a dimensionless pressure-amplitude transmission coefficient. The initial pressure transmitted into the rock mass is then determined as

$$P_t = P_{CJ} \cdot T_p, \tag{6}$$

where P_t represents the initial pressure amplitude transmitted to the rock after explosive–rock coupling. Substituting Equations (4) and (5) into Equation (6), it can be written explicitly as

$$P_t = \frac{2Z_r}{(Z_e + Z_r)} \left(\frac{\rho_e \cdot VoD^2}{(4)} \right). \tag{7}$$

The pressure P_t constitutes the initial condition subsequently used in the propagation model. From this point onward, the decrease in pressure with distance is not represented by a constant efficiency factor but by an attenuation exponent dependent on the mechanical response of the rock mass, as developed in the following sections.

2.3. Geomechanical Characterization of the Rock Mass

The mechanical behavior of an in situ rock mass differs from that of intact-rock specimens because discontinuities, fracturing, alteration, and heterogeneity reduce its effective stiffness. The model incorporates these effects through the equivalent deformation modulus E_{mr}, calculated from intact-rock Young's modulus E_i and RMR. The exponential reduction adopted here is among the empirical correlations reviewed by Vásárhelyi and Kovács [28]:

$$E_{mr} = E_i \, exp\left(\frac{RMR - 100}{36} \right). \tag{8}$$

Here, E_i is the Young's modulus of intact rock and E_{mr} is the estimated deformation modulus of the rock mass. Equation (8) aggregates the effect of rock mass quality through RMR; it does not explicitly model individual discontinuities or apply additional joint factors. Both moduli must use the same units. The initially transmitted pressure is then normalized by this equivalent stiffness:

$$x = \frac{P_t}{E_{mr}}. \tag{9}$$

The index $x = \frac{P_t}{E_{mr}}$ is dimensionless only when P_t and E_{mr} are expressed in the same pressure units. For example, E_{mr} reported in GPa must be multiplied by 1000 when P_t is expressed in MPa; 1 MPa equals 10 bar. The ratio measures the initial loading relative to a stiffness scale and is analogous to a nominal elastic strain scale. E_{mr} is a modulus, not a strength or failure threshold, and x is not a measured strain or a criterion for the onset of plastic failure. In the proposed model, increasing x increases the prescribed attenuation rate.

2.4. Determination of the Attenuation Exponent

Power-law descriptions of blast-wave propagation use an attenuation exponent n to control pressure decay with distance. Conventionally, this exponent is fitted to field records, limiting predictions for uninstrumented sites. Here, a dimensionless exponent is prescribed as a function of the relative dynamic demand x:

$$n_{rm} = 1 + \sqrt{x}. \tag{10}$$

Substituting the definition of x yields

$$n_{rm} = 1 + \sqrt{\frac{P_t}{E_{mr}}}, \tag{11}$$

where n_{rm} is the attenuation exponent associated with the explosive–rock mass system. Because P_t and E_{mr} have the same dimensions, the ratio P_t/E_{mr} is dimensionless and, consequently, n_{rm} is also dimensionless.

Equation (11) makes n_{rm} increase with x. As x tends to zero, n_{rm} approaches 1; increasing x produces faster pressure decay. The square-root relationship produces a sublinear increase. It is a parsimonious modeling assumption rather than a result derived from a constitutive damage law. The limiting value of 1 is a property of this formulation, rather than a universal geometric-spreading exponent: source geometry and propagation regime can change geometric attenuation. Fracturing, joint motion, and other dissipative mechanisms motivate the qualitative dependence, but their individual contributions are not resolved. The model is therefore evaluated within the field conditions considered here, and the assumed exponent remains a limitation discussed in Section 4.3.

2.5. Proposed Model for Estimating Dynamic Pressure

Once P_t and n_{rm} have been determined, pressure propagation is represented by the following power-law. The proposed formulation is denoted M1 throughout this study:

$$P(d) = P_t \cdot \left(\frac{r}{d}\right)^{n_{rm}}, \tag{12}$$

where $P(d)$ is the dynamic pressure estimated at a distance d from the borehole center, P_t represents the initial pressure amplitude transmitted into the rock mass, r is the borehole radius, and n_{rm} is the attenuation exponent determined from the relative dynamic demand of the explosive–rock mass system. Substituting the expression defined for n_{rm} into Equation (12) gives the expanded form of the model:

$$P(d) = P_t \cdot \left(\frac{r}{d}\right)^{1 + \sqrt{\frac{P_t}{E_{mr}}}}. \tag{13}$$

This expression retains the power-law structure used to represent the attenuation of blast-generated waves, but replaces the conventional empirical exponent with a term calculated from the interaction between the initially transmitted pressure and the equivalent rock mass stiffness. Thus, the initial wave magnitude is governed by the explosive characteristics and explosive–rock impedance matching, whereas the rate of pressure decrease with distance depends on the relative dynamic demand P_t/E_{mr}.

The formulation therefore allows pressure–distance curves to be obtained for different combinations of explosive and geomechanical condition without prior calibration of an attenuation exponent from field records. For a given condition, an increase in n_{rm} produces a more rapid decrease in $P(d)$ with distance, whereas values of n_{rm} close to unity represent less pronounced attenuation. Equation (13) is the general expression used in this study to estimate dynamic pressure at different distances and provides the basis for subsequently determining the distance at which the pressure reaches a specific critical threshold.

2.6. Estimation of Critical Distance

Critical distance is the radial distance from the donor borehole center at which the predicted dynamic pressure reaches the operational threshold P_{crit}:

$$P(d_{crit}) = P_{crit}. \tag{14}$$

Substituting Equation (12) into the condition defined by Equation (14) gives

$$P_{crit} = P_t \cdot \left(\frac{r}{d_{crit}}\right)^{n_{rm}}. \tag{15}$$

Dividing Equation (15) by P_t gives $\frac{P_{crit}}{P_t} = (\frac{r}{d_{crit}})^{n_{rm}}$. Taking both sides to the power $\frac{1}{n_{rm}}$ gives $(\frac{P_{crit}}{P_t})^{\frac{1}{n_{rm}}} = \frac{r}{d_{crit}}$. Inverting this relation and multiplying by r yields

$$d_{crit} = r \cdot \left(\frac{P_t}{P_{crit}}\right)^{\frac{1}{n_{rm}}}. \tag{16}$$

Substituting $n_{rm} = 1 + \sqrt{\frac{P_t}{E_{mr}}}$ from Equation (11) into the exponent $\frac{1}{n_{rm}}$ in Equation (16) yields Equation (17). Thus, the exponent is the reciprocal of the entire quantity $1 + \sqrt{\frac{P_t}{E_{mr}}}$:

$$d_{crit} = r \cdot \left(\frac{P_t}{P_{crit}}\right)^{\frac{1}{1+\sqrt{\frac{P_t}{E_{mr}}}}}. \tag{17}$$

Equation (17) is the final expression for estimating the critical distance for pressure transmission. The formulation integrates the initially transmitted pressure P_t, determined from explosive properties and explosive–rock impedance matching, with the equivalent rock mass stiffness E_{mr}, used to determine the attenuation exponent. Thus, d_{crit} can be calculated for different pressure thresholds without prior calibration of a condition-specific empirical attenuation exponent.

The analysis uses two distinct pressure criteria. For the WebGen™ 200 (Orica Limited, East Melbourne, Australia) cases, 200 bar (20 MPa) is the manufacturer-reported dynamic-shock survival level of the WebGen™ Primer while in listening mode [29]. For the conventional i-kon™ III (Orica Limited, East Melbourne, Australia) electronic-detonator cases, 1200 bar (120 MPa) is the operational threshold used in the evaluated field dataset. The supporting manufacturer documentation is commercially sensitive and is not publicly available; consequently, the value cannot be cited here as a publicly documented manufacturer qualification. It is retained only as a dataset-specific operational criterion and is not

presented as an independently verified or universal product tolerance. Neither criterion is derived from Equation (17), and the 200 bar rating is specific to the cited product, operating mode, and technical data sheet rather than a universal failure pressure for wireless detonators. Product-specific qualification and test conditions must be consulted before transferring either criterion to another initiation system. The exterior-domain interpretation of Equation (17) requires $P_t > P_{crit} > 0$ and $d_{crit} \geq r$; if $P_t \leq P_{crit}$, the threshold is already met at the borehole wall.

2.7. Study Area and Operational Context

The model was evaluated with information from three Chilean underground mines: El Teniente (panel caving), Chuquicamata Underground (block caving), and Pucobre (sublevel stoping). The lithological labels used in the operational dataset are andesite from the Complejo Máfico El Teniente (CMET), Cuarzo Igual Sericita (QIS), and metandesite. The cases provide contrasting combinations of equivalent stiffness, dynamic rock properties, and explosive characteristics. Site-specific depth and in situ stress were not included as quantitative variables in the compiled model inputs, so differences among the cases cannot be attributed quantitatively to confinement.

The geological names require some qualification. In Chuquicamata, QIS describes a subunit of quartz-sericite-altered rock, rather than a distinct primary igneous lithology. Published mine descriptions identify pervasive secondary quartz and sericite, with anhydrite and minor gypsum [30]. At El Teniente, the historical operational label "andesite" is retained here for CMET; geological descriptions characterize the host complex as altered mafic intrusive rocks, including gabbros, diabases, and porphyritic basalts to basaltic andesites, with plagioclase and widespread biotite alteration [31]. The Punta del Cobre Formation contains andesitic volcanic rocks and volcaniclastic units [32]. These published descriptions provide regional and mine context; they do not establish the modal mineralogy or alteration intensity of the particular test specimens.

The input data combine existing mine information and field-campaign records. Rock density, Young's modulus, P-wave velocity, strength properties, and RMR were compiled from geotechnical and geological information supplied by the respective mine departments. E_{mr} was calculated with Equation (8), rather than measured independently in the blasting campaigns. Drilling geometry came from the operational designs. Explosive density was recorded during loading, VoD was recorded for the field trials, and dynamic pressure was measured in the receptor boreholes. Tables 1–3 summarize the compiled geomechanical and operational information, which should be distinguished from the newly recorded pressure observations. The pressure records provided the experimental basis for the critical-distance comparisons presented in Section 3.3.

Table 1. Equivalent geomechanical properties and experimental critical distance for the evaluated lithologies.

Lithology	*RMR*	E_{mr} (GPa)	σ_{mr} (MPa)	Calculated Strain ε_{mr}(%)	Distance (m)
QIS	67	11.7	0.8	0.0068	0.40
Metandesite	51	33.7	1.4	0.0042	0.85
Andesite CMET	71	25.5	3.8	0.0149	0.55

Table 2. Comparison of intact-rock properties with the equivalent rock mass properties estimated using the RMR index.

Lithology	RMR	E (GPa)	σ_t (MPa)	E_{mr} (GPa)	σ_{mr} (MPa)	Calculated Strain ε_i(%)	Calculated Strain ε_{mr}(%)
QIS	67	29.2	2.6	11.7	0.8	0.0089	0.0068
Metandesite	51	131.4	8.7	33.7	1.4	0.0066	0.0042
Andesite CMET	71	57.0	11.0	25.5	3.8	0.0193	0.0149

Table 3. Physical and operational parameters used as input variables for the proposed model.

Parameter	Metandesite (Pucobre)	QIS (Chuquicamata Underground)	Andesite (El Teniente)
RMR	51 (Fair)	67 (Good)	71 (Good)
Tensile strength (σ_t)	8.67 MPa	2.56 MPa	11.00 MPa
Young's modulus (E)	131.4 GPa	29.2 GPa	57.0 GPa
Density (ρ)	2.85 g/cm^3	2.70 g/cm^3	2.80 g/cm^3
P-wave velocity (V_p)	6751 m/s	4656 m/s	5747 m/s
Explosive (Type)	Subtek Control bulk emulsion	Subtek Control bulk emulsion	ANFO
Velocity of Detonation (VoD)	5141 m/s	5077 m/s	4388 m/s
Borehole diameter (ϕ)	0.0762 m	0.0762 m	0.0762 m
Burden (B)	2.0 m	1.7 m	2.5 m

The bulk emulsion used in the field tests was Subtek Control (Orica Limited, East Melbourne, Australia).

2.8. Field Tests

The three campaigns used a common normalized donor–receptor layout, with receptor positions at ¼B, ½B, ¾B, and B (Figure 1). The elevation scheme in Figure 2 shows a 10 m donor hole with a 7 m charge column and 3 m stemming, and 8 m receptor holes with 5 m charge columns and 3 m stemming. Pressure sensors and backup electronic detonators were positioned as illustrated in Figure 2. According to Table 3, the borehole diameter was 0.0762 m at all three sites; Pucobre and Chuquicamata used Subtek Control bulk emulsion, whereas El Teniente used ANFO. Thus, the normalized arrangement was shared, while absolute receptor separations depended on B and explosive properties differed among sites.

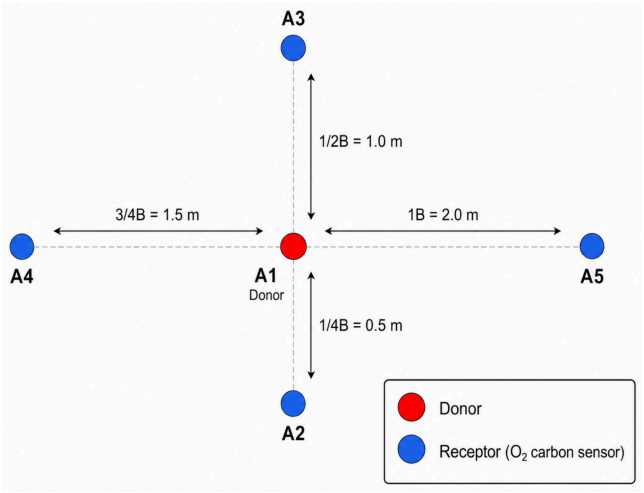


Figure 1. Plan view of the normalized donor–receptor layout, illustrated for a design burden B = 2.0 m. The central donor borehole A1 is shown in red, and receptor boreholes A2–A5 are shown in blue at the fractions of B indicated in the diagram; B denotes the site-specific design burden.

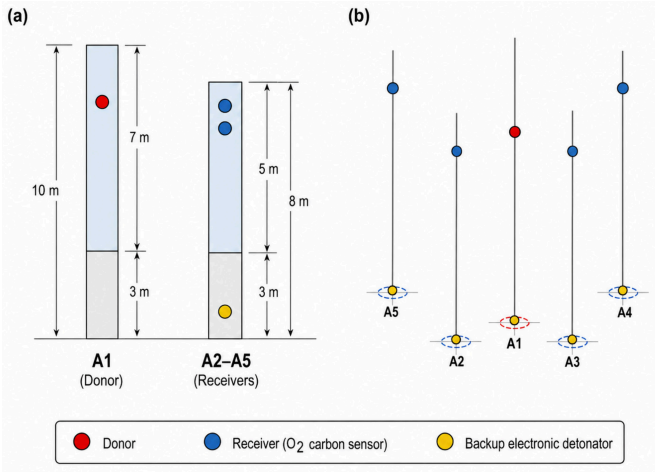


Figure 2. Experimental configuration: (**a**) a 10 m donor borehole (A1) with a 7 m charge column and 3 m of stemming, and 8 m receptor boreholes (A2–A5) with 5 m charge columns and 3 m of stemming; (**b**) relative positions of the donor, pressure sensors, and backup electronic detonators. Red, blue, and yellow symbols denote the donor, pressure sensors, and backup electronic detonators, respectively.

During the campaigns, explosive properties and dynamic pressures in receptor boreholes were recorded. Pressure–distance relationships were used to identify separations associated with the specified operational thresholds. These field-derived distances were compared with the model estimates. Records at 200 bar extended the evaluation to lower pressure levels and greater distances. The experimental reference distances depend on the processing of the measured pressure–distance records, as illustrated by the fitted Pucobre curve in Figure 3.

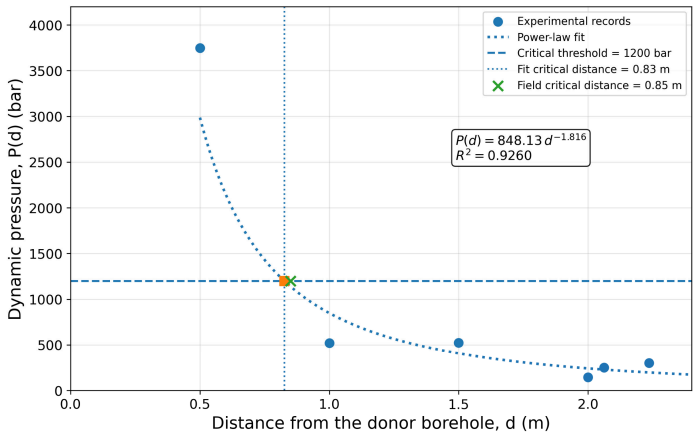


Figure 3. Dynamic pressure versus distance from the donor borehole for Pucobre (metandesite). Blue circles show the experimental records, the dotted curve is the power-law fit, the horizontal dashed line marks the 1200 bar threshold, the orange square marks the intersection of the fitted curve with this threshold at approximately 0.83 m, also indicated by the vertical dotted line, and the green cross marks the field-derived critical distance of 0.85 m.

Data analysis was performed using the latest version of Python (Python Software Foundation, Beaverton, OR, USA) available at the time of analysis.

For comparative purposes, experimental data were also used to evaluate the classical power-law relationship in Equation (1). Critical distances estimated using the proposed model were compared with those determined from field records by evaluating the relative error for each condition and the overall model behavior under the different geomechanical conditions considered.

3. Results

3.1. Characterization of the Study Cases

Consistent with the study area and operational context described in Section 2.7, the model was evaluated using information from three Chilean underground mines: El Teniente (andesite); Chuquicamata Underground, represented by the basic geotechnical unit Cuarzo Igual Sericita (QIS); and Pucobre (metandesite). The cases were selected to contrast different combinations of physical, mechanical, and dynamic rock properties, equivalent rock mass stiffness, and explosive characteristics. Although the three rock masses exhibit RMR values between 51 and 71, their mechanical properties show marked contrasts. Metandesite has the highest equivalent deformation modulus (33.7 GPa), followed by andesite (25.5 GPa) and QIS (11.7 GPa), an ordering that does not coincide with RMR.

Tables 1 and 2 distinguish calculated nominal strain at intact-rock and rock mass scales. With tensile-strength magnitudes σ_t and σ_{mr}, these proxies are $\varepsilon_i = \frac{\sigma_t}{E_i}$ and $\varepsilon_{mr} = \frac{\sigma_{mr}}{E_{mr}}$. Percent values are calculated as $\frac{100\sigma}{E}$ after conversion to common units. For example, QIS gives $100 \times \frac{0.8}{1000 \times 11.7} = 0.0068\%$ at the rock mass scale. The former headings "Test Deformation" and "Deformation" have been replaced because these ratios are calculated quantities, not independent measurements of transient strain during blasting. Values are computed from the rounded strength and modulus entries shown in Table 2. These descriptive ratios do not enter Equations (9)–(17).

Table 2 shows that the same gradient is observed in the Young's modulus of intact rock: 131.4 GPa for metandesite, 57.0 GPa for andesite, and 29.2 GPa for QIS. Scaling to the equivalent deformation modulus (E_{mr}) incorporates rock mass condition into the relative dynamic demand P_t/E_{mr}, rather than representing the dynamic response solely through intact rock properties or RMR.

The reported E_i of 131.4 GPa for Pucobre is high and has a strong influence on the resulting E_{mr}. The rock mass value of 33.7 GPa follows from Equation (8) using RMR = 51. The large modulus and P-wave velocity distinguish this input dataset, but the lithological label alone does not demonstrate their cause. A specific attribution to recrystallization, alteration, or confinement requires specimen-level evidence and a documented modulus measurement method; static and dynamic moduli should not be treated as interchangeable.

Table 3 completes the characterization with the physical, dynamic, and operational properties. P-wave velocities are 6751, 5747, and 4656 m/s for metandesite, andesite, and QIS, respectively; together with rock density, these differences govern impedance. Pucobre and Chuquicamata Underground use Subtek Control bulk emulsion (VoD values of 5141 and 5077 m/s), whereas El Teniente uses ANFO (4388 m/s).

Overall, the three cases define a physical, mechanical, and dynamic gradient: metandesite at the high stiffness and high-P-wave-velocity end, andesite under intermediate conditions, and QIS at the lower end. This configuration enables evaluation of the initial transmission, governed by impedance contrast, and attenuation, associated with equivalent rock mass stiffness.

3.2. Field Experimental Results

The field-derived critical distances at 1200 bar were 0.40 m in QIS, 0.85 m in metandesite, and 0.55 m in andesite. At the manufacturer-reported 200 bar dynamic-shock survival level for the WebGen™ 200 Primer in listening mode [29], the field-derived distances were 1.10 m in QIS and 1.75 m in andesite. In each case, critical distance denotes the donor–receptor separation associated with the specified pressure criterion; lowering the criterion shifts this separation outward.

Figure 3 shows the Pucobre results. Measured pressure decreases with distance, and the power-law fit crosses the 1200 bar threshold at approximately 0.83 m, close to the field-

derived critical distance of 0.85 m. Applying a 20% safety factor gives a minimum design distance of 1.0 m.

Figure 4 compares the pressure–distance curves predicted by the M1 model with the field-observed critical distances for the three conditions. The curves show different attenuation rates and the shift in critical distance as the pressure threshold changes; the 200 bar data extend the evaluation to greater distances.

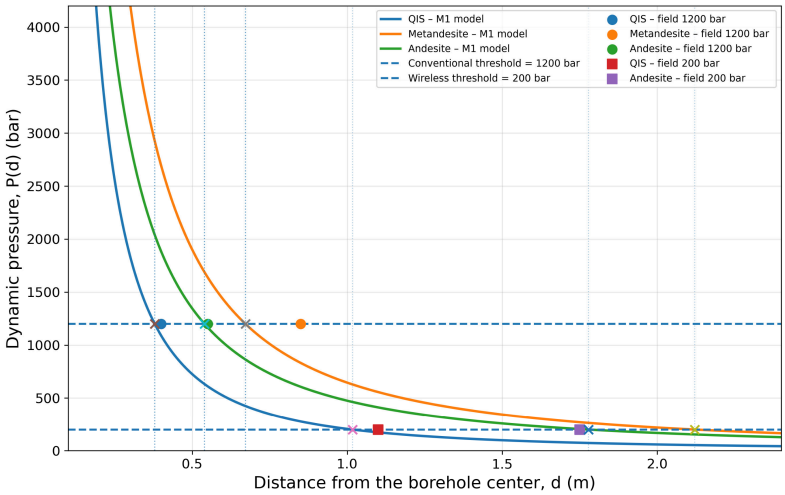


Figure 4. Dynamic pressure–distance curves predicted by the proposed model (M1) for QIS (Chuquicamata Underground), metandesite (Pucobre), and andesite (El Teniente). Solid curves show the predictions, dashed horizontal lines mark the 1200 and 200 bar thresholds, crosses indicate the intersections of the model curves with these thresholds, circles represent field-derived critical distances at 1200 bar, and squares represent field-derived critical distances at 200 bar. QIS denotes Cuarzo Igual Sericita.

3.3. Model Validation Against Field Data

Predictive performance was evaluated using five experimental conditions combining the three lithologies and two critical pressure levels. Table 4 presents the observed critical distances, model estimates, and relative errors for each case.

Table 4. Comparison of field-observed critical distances with those estimated using the proposed model.

(Mine/Lithology)	P Critic (Bar)	Critical Distance (Field)	Critical Distance (Model)	Relative Error (%)
Chuquicamata Underground (QIS)	1200	0.40 m	0.379 m	5.25
Pucobre (Metandesite)	1200	0.85 m	0.679 m	20.12
El Teniente (Andesite)	1200	0.55 m	0.537 m	2.36
Chuquicamata Underground (QIS)	200	1.10 m	0.958 m	12.91
El Teniente (Andesite)	200	1.75 m	1.776 m	1.49

To quantify the differences between model predictions and field observations, relative error was calculated as

$$Relative\ error\ (\%) = 100 \times \frac{\left|d_{model} - d_{field}\right|}{d_{field}} \tag{18}$$

Here, d_{model} and d_{field} denote the predicted and field-derived critical distances, respectively. Absolute relative errors were 5.25%, 20.12%, and 2.36% for QIS, metandesite, and andesite at 1200 bar, and 12.91% and 1.49% for QIS and andesite at 200 bar. Across the five conditions, the mean absolute relative error was 8.43% and RMSE was 0.101 m. The largest

deviation occurred for Pucobre: 0.679 m predicted versus 0.85 m observed. At 200 bar, andesite gave 1.776 m predicted versus 1.75 m observed. These results indicate agreement within the evaluated dataset, with individual errors ranging from 1.49% to 20.12%.

3.4. Parametric Analysis of RMR and Pressure Threshold

Figures 5–7 show the parametric response of critical distance to RMR for different pressure thresholds. Holding the remaining properties of each case constant, an increase in RMR increases E_{mr}, reduces P_t/E_{mr}, and decreases the attenuation exponent; consequently, pressure attenuates more slowly and a greater distance is required to reach a given threshold. Critical distance also increases systematically as the threshold decreases, with the effect being most pronounced at 200 bar. These curves should be interpreted as a parametric analysis of the formulation rather than as a universal relationship between RMR and critical distance because Young's modulus, density, P-wave velocity, and explosive properties vary simultaneously among lithologies.

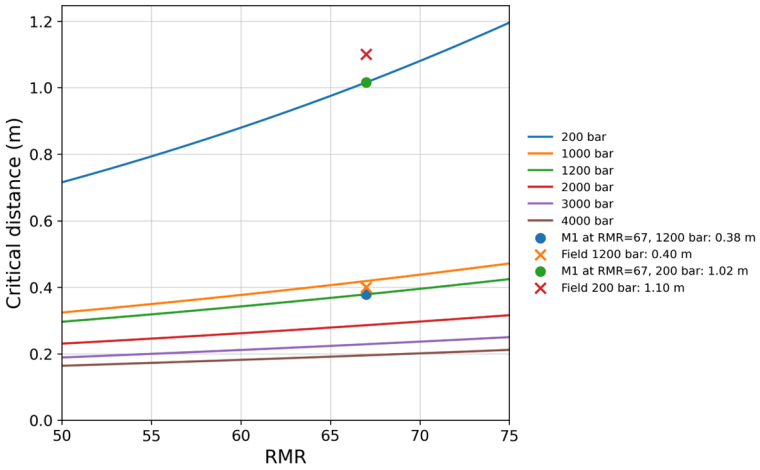


Figure 5. Critical distance predicted by the proposed model (M1) as a function of Rock Mass Rating (RMR) for QIS (Chuquicamata Underground), with the other input properties held constant. Colored curves represent pressure thresholds from 200 to 4000 bar; circles and crosses identify the M1 and field-derived distances at RMR = 67 for the 1200 and 200 bar cases, as listed in the legend. QIS denotes Cuarzo Igual Sericita.

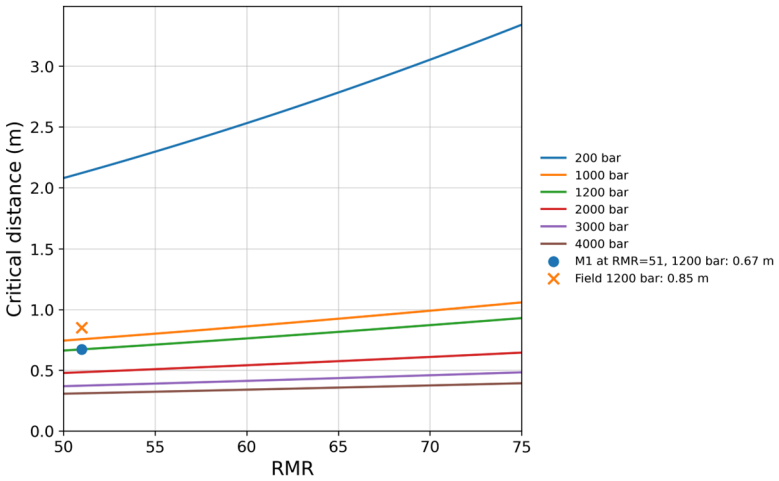


Figure 6. Critical distance predicted by the proposed model (M1) as a function of Rock Mass Rating (RMR) for metandesite (Pucobre), with the other input properties held constant. Colored curves represent pressure thresholds from 200 to 4000 bar; the circle and cross identify the M1 and field-derived distances at RMR = 51 and 1200 bar, as listed in the legend.

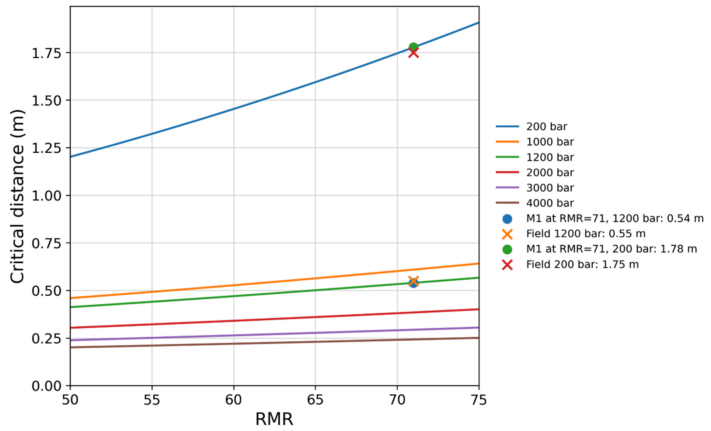


Figure 7. Critical distance predicted by the proposed model (M1) as a function of Rock Mass Rating (RMR) for andesite (El Teniente), with the other input properties held constant. Colored curves represent pressure thresholds from 200 to 4000 bar; circles and crosses identify the M1 and field-derived distances at RMR = 71 for the 1200 and 200 bar cases, as listed in the legend.

4. Discussion

Across five field-derived critical distances, the model gave a mean absolute relative error of 8.43% and RMSE of 0.101 m. This supports its use for preliminary comparisons within the tested domain without establishing a universal attenuation law. Explosive and rock impedances determine P_t, while E_{mr} controls the prescribed attenuation exponent through $\frac{P_t}{E_{mr}}$. RMR therefore contributes indirectly through stiffness rather than serving as a standalone predictor. This interpretation is consistent with research on the combined effects of source characteristics and rock mass structure [14–17].

4.1. Influence of Geomechanical and Lithological Properties

Pucobre combines the lowest RMR (51) with the highest reported E_i (131.4 GPa), P-wave velocity (6751 m/s), and E_{mr} (33.7 GPa). Andesite is intermediate and QIS has the lowest equivalent stiffness. QIS is a quartz-sericite alteration subunit [30], whereas the Pucobre and CMET labels refer to different geological settings [31,32]. Alteration and discontinuities can influence stiffness and transmission, but published regional descriptions do not establish a unique mineralogical cause for these particular measurements. The high Pucobre modulus should therefore be interpreted as a site input requiring documented characterization.

The largest error, 20.12% for Pucobre, shows that the equivalent-medium representation leaves local variability unresolved. Joint geometry, confinement, and stress can modify transmission and scattering [15–17,33,34]. Their contributions cannot be separated here because site-specific depth and in situ stress are not included in the dataset. The 200 bar comparisons extend the tested distance range, but they remain two observations rather than evidence of general validity at low pressure.

4.2. Operational Scope of the Model

The formulation uses pre-blast properties to estimate the distance associated with a selected pressure threshold. It can support preliminary planning where attenuation records are unavailable, and subsequent monitoring can be used to evaluate local behavior. Predicted distance increases when the threshold decreases from 1200 to 200 bar. These distances are conditional estimates; they do not establish product tolerances or replace the operational assessment of initiation-system performance. The model underestimates four of the five reported field distances, so close average agreement alone does not establish a conservative design margin.

4.3. Limitations and Future Work

The dataset comprises three lithological conditions and five threshold-distance observations. Validation should be expanded before extrapolation to other rock masses, explosives, diameters, or loading configurations. The square-root attenuation function is an assumed relationship, and E_{mr} is obtained from an empirical correlation rather than a dynamic constitutive law. Individual discontinuities, confinement, in situ stress, water, and three-dimensional heterogeneity are not explicitly represented. Future work should quantify input uncertainty, prediction intervals, and the sensitivity to modulus measurement methods. With larger datasets, data-driven surrogates such as those discussed in Section 1 [24,26,27] could complement the explicit formulation; the present five observations are insufficient for a meaningful machine-learning benchmark.

5. Conclusions

A formulation combining detonation pressure, impedance matching, and equivalent rock mass stiffness was evaluated for estimating critical pressure-transmission distances in underground blasting. Its attenuation exponent is prescribed as a function of $\frac{P_t}{E_{mr}}$, avoiding separate site-specific exponent fitting while retaining empirical and assumed model components. Five conditions from Chuquicamata Underground, Pucobre, and El Teniente gave a mean absolute relative error of 8.43% and RMSE of 0.101 m. Individual errors ranged from 1.49% to 20.12%, with the largest deviation in Pucobre. The comparisons indicate that RMR alone does not determine critical distance: it acts through E_{mr}, alongside the explosive and rock properties that determine P_t. The model can support preliminary assessment within the evaluated conditions. Broader field validation, documented input uncertainty, and consideration of discontinuities and stress are needed to establish its applicability and prediction reliability.

Author Contributions: Conceptualization, A.D. and L.Á.; methodology, L.Á., A.D. and H.H.; software, A.D., C.T. and L.Á.; validation, H.H., E.A. and C.T.; formal analysis, A.D., L.Á. and H.H.; investigation, A.D. and L.Á.; resources, A.D., C.T. and H.H.; data curation, A.D., H.H. and E.A.; writing—original draft preparation, A.D. and L.Á.; writing—review and editing, H.H., C.T. and E.A.; visualization, A.D. and H.H.; supervision, E.A., L.Á. and H.H.; project administration, A.D. and H.H. All authors have read and agreed to the published version of the manuscript.

Funding: This research received no external funding.

Data Availability Statement: Data supporting the findings of this study are available from the corresponding author upon reasonable request.

Conflicts of Interest: Author Alejandro Díaz was employed by the company Orica S.A. The remaining authors declare that the research was conducted in the absence of any commercial or financial relationships that could be construed as a potential conflict of interest.

Abbreviations

The following abbreviations are used in this manuscript:

ANFO	Ammonium Nitrate Fuel Oil
CMET	Complejo Máfico El Teniente
DeepONet	Deep operator network
QIS	Cuarzo Igual Sericita
RMR	Rock Mass Rating
RMSE	Root Mean Square Error
PPV	Peak Particle Velocity
VoD	Velocity of Detonation
M1	Proposed pressure attenuation and critical-distance model

Nomenclature

Symbol	Definition	Unit
$P(d)$, P	Dynamic pressure at distance d	MPa or bar
P_d	Borehole detonation pressure in Equation (1)	MPa or bar
P_{CJ}	Approximate Chapman–Jouguet pressure	MPa or bar
P_t, P_{crit}	Initially transmitted pressure; selected threshold	MPa or bar
E_i, E	Intact-rock Young's modulus	GPa or MPa
E_{mr}	Equivalent rock mass deformation modulus	GPa or MPa
σ_t, σ_{mr}	Intact-rock and rock mass tensile-strength magnitudes	MPa
ε_i, ε_{mr}	Calculated nominal strain at the two scales	Dimensionless; %
ρ_e, ρ_r	Explosive and rock densities	kg/m^3
VoD, V_p	Detonation and compressional-wave velocities	m/s
Z_e, Z_r	Explosive and rock characteristic impedances	kg/(m^2 s)
T_p	Pressure-amplitude transmission coefficient	Dimensionless
x	Relative dynamic demand $\frac{P_t}{E_{mr}}$	Dimensionless
n, n_{rm}	Empirical and proposed attenuation exponents	Dimensionless
r, ϕ	Borehole radius and diameter; $\phi = 2r$	m
d, d_{crit}	Radial distance and critical radial distance	m
d_{model}, d_{field}	Predicted and field-derived critical distances	m
B	Design burden	m
RMR	Rock Mass Rating	Dimensionless

References

1. Ding, C.; Yang, R.; Chen, C.; Zhu, X.; Feng, C.; Xie, Q. Space-Time Effect of Blasting Stress Wave and Blasting Gas on Rock Fracture Based on a Cavity Charge Structure. *Int. J. Rock Mech. Min. Sci.* **2022**, *160*, 105238. [CrossRef]
2. Díaz, A.; Hernández, H.; Gallo, J.; Álvarez, L. A Theoretical Model for Predicting the Blasting Energy Factor in Underground Mining Tunnels. *Mining* **2026**, *6*, 2. [CrossRef]
3. Huo, X.; Shi, X.; Qiu, X.; Zhou, J.; Gou, Y.; Yu, Z.; Zhang, S. A Study on Raise Blasting and Blast-Induced Vibrations in Highly Stressed Rock Masses. *Tunn. Undergr. Space Technol.* **2022**, *123*, 104407. [CrossRef]
4. Leng, Z.; Fan, Y.; Lu, W.; Gao, Q.; Yang, G. Failure Mechanisms of Electronic Detonators Subjected to High Impact Loading in Rock Drilling and Blasting. *Int. J. Coal Sci. Technol.* **2025**, *12*, 10. [CrossRef]
5. Álvarez, L.; Hernández, H.; Alberdi, E.; Goti, A. Enhanced Short-Term Scheduling of Underground Mining Activities Using Tabu Search: A Comparative Analysis. *Contemp. Math.* **2025**, *6*, 7925–7949. [CrossRef]
6. Langefors, U.; Kihlström, B. *The Modern Technique of Rock Blasting*; Wiley: Hoboken, NJ, USA, 1963.
7. Holmberg, R.; Persson, P.A. The Swedish Approach to Contour Blasting. In *Proceedings of the 4th Conference on Explosives and Blasting Technique, New Orleans, LA, USA, 1 February 1978*; IEEE: New York, NY, USA, 1978; pp. 113–127.
8. Wang, X.; Li, J.; Zhao, X.; Liang, Y. Propagation Characteristics and Prediction of Blast-Induced Vibration on Closely Spaced Rock Tunnels. *Tunn. Undergr. Space Technol.* **2022**, *123*, 104416. [CrossRef]
9. Persson, P.-A.; Holmberg, R.; Lee, J. *Rock Blasting and Explosives Engineering*; CRC Press: Boca Raton, FL, USA, 1994.
10. Yilmaz, O.; Unlu, T. An Application of the Modified Holmberg-Persson Approach for Tunnel Blasting Design. *Tunn. Undergr. Space Technol.* **2014**, *43*, 113–122. [CrossRef]
11. Ye, Z.; Yang, J.; Yao, C.; Zhang, X.; Jiang, S.; Zhou, C. Attenuation Characteristics of Shock Waves in Drilling and Blasting Based on Viscoelastic Wave Theory. *Int. J. Rock Mech. Min. Sci.* **2023**, *171*, 105573. [CrossRef]
12. Hemphill, G.B. *Blasting Operations*; McGraw-Hill: New York, NY, USA, 1981.
13. Zhang, Z.X.; Gong, F.; Kozlovskaya, E.; Aladejare, A. Characteristic Impedance and Its Applications to Rock and Mining Engineering. *Rock Mech. Rock Eng.* **2023**, *56*, 3139–3158. [CrossRef]
14. Zhou, Z.; Wang, Z.; Cheng, R.; Wang, J. Experimental and Numerical Study on Blast-Induced Rock Damage and Fragmentation under Low Temperatures. *Eng. Fail. Anal.* **2025**, *174*, 109497. [CrossRef]
15. Cai, Y.; Xu, Z.; Liu, Y.; Chen, X.; Qi, W.; Liu, L. Weakly Confined Slotted Cartridge Blasting in Jointed Rock Mass. *Theor. Appl. Fract. Mech.* **2024**, *134*, 104695. [CrossRef]
16. Lin, Q.; Zhu, X.; Yuan, J.; Feng, C.; Gan, Y.; Jiao, W.; Zhang, Y. A Hybridized Continuum-Discontinuum Modeling for Investigating the Fracture and Energy Evolution Characteristics of Rock Mass under Sequential Explosive Detonation Using a Bilinear Cohesive Fracture Model. *Comput. Geotech.* **2023**, *162*, 105607. [CrossRef]
17. Liu, S.; Kou, M.; Wang, Z.; Zhang, Y.; Liu, F. A Phase-Field Model for Blasting-Induced Failure and Breakage Analysis in Rock Masses. *Int. J. Rock Mech. Min. Sci.* **2024**, *177*, 105734. [CrossRef]

18. Fan, Z.; Zhang, J.; Xu, H.; Wang, X. Transmission and Application of a P-Wave across Joints Based on a Modified g-λ Model. *Int. J. Rock Mech. Min. Sci.* **2022**, *150*, 104991. [CrossRef]
19. Bieniawski, Z.T. *Engineering Rock Mass Classifications: A Complete Manual for Engineers and Geologists in Mining, Civil, and Petroleum Engineering*; John Wiley & Sons: New York, NY, USA, 1989.
20. Zhang, B.; Mu, J.; Zheng, J.; Lv, Q.; Deng, J. A New Estimation Method and an Anisotropy Index for the Deformation Modulus of Jointed Rock Masses. *J. Rock Mech. Geotech. Eng.* **2022**, *14*, 153–168. [CrossRef]
21. Gou, Y.; Shi, X.; Yu, Z.; Huo, X.; Qiu, X. Evaluation of Underground Blast-Induced Ground Motions through near-Surface Low-Velocity Geological Layers. *J. Rock Mech. Geotech. Eng.* **2023**, *15*, 600–617. [CrossRef]
22. He, B.; Armaghani, D.J.; Lai, S.H.; He, X.; Asteris, P.G.; Sheng, D. A deep dive into tunnel blasting studies between 2000 and 2023—A systematic review. *Tunn. Undergr. Space Technol.* **2024**, *147*, 105727. [CrossRef]
23. Zhu, Y.; Chen, Z.; Onederra, I. A maximum velocity mapping approach for damage prediction in underground tunnelling destressing blasting. *Tunn. Undergr. Space Technol.* **2026**, *177*, 107922. [CrossRef]
24. Zhou, J.; Asteris, P.G.; Armaghani, D.J.; Pham, B.T. Prediction of ground vibration induced by blasting operations through the use of the Bayesian Network and random forest models. *Soil Dyn. Earthq. Eng.* **2020**, *139*, 106390. [CrossRef]
25. Stochino, F.; Nocera, F.; Gardoni, P. Physics-based Demand Model and Fragility Functions of Industrial Tanks under Blast Loading. *J. Loss Prev. Process Ind.* **2022**, *77*, 104798. [CrossRef]
26. Drosopoulos, G.A.; Stavroulakis, G.E. DeepONet for the Prediction of Failure Response of a Two-Dimensional Fibre-Reinforced Composite Plate. *Bull. Comput. Intell.* **2025**, *1*, 76–88. [CrossRef]
27. Bardhan, A.; Kardani, N. An Efficient Meta-Ensemble Paradigm for Modelling Poisson's Ratio and Maximum Horizontal Stress in Casing Collapse Hazard. *Bull. Comput. Intell.* **2026**, *2*, 146–163. [CrossRef]
28. Vásárhelyi, B.; Kovács, D. Empirical methods of calculating the mechanical parameters of the rock mass. *Period. Polytech. Civ. Eng.* **2017**, *61*, 39–50. [CrossRef]
29. Orica. *WebGen™ 200: Sistema Electrónico Inalámbrico de Voladura*; Ficha de datos técnicos TDES-W0201-00-001_WG200; Orica: Melbourne, Australia, 2022.
30. Divasto, C.; Barindelli, G.; Pereira, J. Methodology for creating and calibrating DFN models from digital terrain models in underground mining, Chuquicamata underground case study. In *Proceedings of the MassMin 2024, Kiruna, Sweden, 17–19 September 2024*; Luleå University of Technology: Luleå, Sweden, 2024; pp. 249–266. [CrossRef]
31. Skewes, M.A.; Arévalo, A.; Floody, R.; Zuñiga, P.H.; Stern, C.R. The El Teniente Megabreccia Deposit, the World's Largest Copper Deposit. In *Super Porphyry Copper & Gold Deposits: A Global Perspective*; Porter, T.M., Ed.; PGC Publishing: Adelaide, Australia, 2005; Volume 1, pp. 83–113.
32. Marschik, R.; Fontboté, L. The Punta del Cobre Formation, Punta del Cobre–Candelaria area, northern Chile. *J. S. Am. Earth Sci.* **2001**, *14*, 401–433. [CrossRef]
33. Huo, X.; Jiang, Y.; Wei, W.; Qiu, X.; Yu, Z.; Nong, J.; Li, Q. Three-Dimensional Finite Element Simulation and Reconstruction of Jointed Rock Masses for Bench Blasting. *Simul. Model. Pract. Theory* **2024**, *135*, 102975. [CrossRef]
34. Xu, R.; Huang, X.; Xie, L. Study on the Blasting-Induced Damage Characteristics of Rock Mass Considering Spatial Variability. *Eng. Fract. Mech.* **2025**, *327*, 111489. [CrossRef]

Disclaimer/Publisher's Note: The statements, opinions and data contained in all publications are solely those of the individual author(s) and contributor(s) and not of MDPI and/or the editor(s). MDPI and/or the editor(s) disclaim responsibility for any injury to people or property resulting from any ideas, methods, instructions or products referred to in the content.